A&A 511, A83 (2010)
DOI: 10.1051/0004-6361/200810224

Astronomy & Astrophysics

Multi-wavelength observations of a giant flare on CN Leonis

II. Chromospheric modelling with PHOENIX⋆

B. Fuhrmeister, J. H. M. M. Schmitt, and P. H. Hauschildt

Hamburger Sternwarte, University of Hamburg, Gojenbergsweg 112, 21029 Hamburg, Germany
e-mail: bfuhrmeister@hs.uni-hamburg.de

Received 20 May 2009 / Accepted 15 December 2009

ABSTRACT

Aims. In M dwarfs, optical emission lines and continua are sensitive to changing chromospheric conditions, e.g., during flares. To study flare conditions for an observed spectrum, a comparison to synthesised spectra from model atmospheres is needed.
Methods. Using the stellar atmosphere code PHOENIX, we computed a set of 41 1D NLTE parameterised chromospheric models including the photosphere and parts of the transition region. By comparison of a linear combination of the synthesised spectra and a quiescent (observed) chromosphere to observed UVES/VLT spectra of a giant flare of the M 5.5 dwarf CN Leo (Gl406), we find the best-fitting flare model chromosphere.
Results. Our model spectra give a fairly good overall description of the observed continua and emission lines. In the best-fitting model, the temperature minimum is deep in the atmosphere resulting in high electron pressure for the chromospheric flaring area. The inferred chromospheric filling factor of the flare is about 3 percent, which declines during the flare. The photospheric flare filling factor is about 0.3 percent.

Key words. stars: atmospheres – stars: late-type – stars: individual: CN Leonis – stars: chromospheres – stars: flare

1. Introduction

Flaring is a commonly observed phenomenon in late-type stars. Flares are observed at radio, sometimes even IR, optical, and UV, as well as at X-ray wavelengths. Obviously some additional energy, probably derived from magnetic re-connection events, is emitted over a wide range of the electromagnetic spectrum. Optical flare spectra typically probe the reaction of the chromospheric emission lines and the continuum emission in the very blue optical range most probably originating in the photosphere (Hawley & Fisher 1992). Since these two features probe different parts of the atmosphere, the emission line maximum is usually delayed with respect to the continuum emission. As far as chromospheric emission lines are concerned, the spectrum of H I plays a particularly important role, since the ionisation fraction of H I partly determines the outer atmospheric structure. However, strong emission lines from neutral or singly ionised metals, which are typically found in the optical, also provide valuable insight into the flare process, since these lines probe different layers of the atmosphere. The use of these metal lines does complicate the model calculations, since NLTE effects have to be taken into account (e.g. Falchi & Mauas 1998; Fuhrmeister et al. 2006).

A self-consistent model of a flare requires a time-dependent treatment of the coupled hydrodynamic and radiative transport equations and the equation of state in 3 dimensions. This is a cumbersome computational problem, and even realistic 1D coupled radiative and hydro-dynamical models of solar/stellar flares are lacking, although some steps have already been performed in this direction (Allred et al. 2005, 2006). Another simpler approach to a first understanding of the flare phenomenon is to use 1D chromospheric models with a semi-empirical or parameterised temperature rise. The first attempt in this direction were carried out by Cram & Woods (1982), who computed a grid of models of flaring chromospheres for M dwarfs. Houdebine (1992) built a grid of chromospheric model atmospheres for M dwarfs to study the influence of different model parameters on the emerging spectra. For a single flare on AD Leo, Mauas & Falchi (1994) computed semi-empirical chromospheric models assuming different filling factors and found that filling factors between 1 and 5 percent resulted in fairly good agreement between their computed and observed spectral features.

Using a somewhat different approach that also includes the corona and the transition region, Hawley & Fisher (1992) computed a set of five model atmospheres and compared the resulting line and continuum fluxes to a giant flare of AD Leo. These authors were unable to describe all aspects of the flare with a single model, so they had to introduce additional heating to the upper chromosphere to match the Ca II and Balmer line emission.

The basic problem with all 1D chromospheric models with a fixed temperature rise is the static and averaged description of a phenomenon being dynamical in space and time. The same is true for the observations, since spectra are normally integrated over the whole stellar surface and over significant exposure times. Despite these severe limitations of our simple models we hope to gain some understanding of the properties of a flaring atmosphere. We restricted ourselves to the study of parametrised flare models, though.

⋆ Based on observations collected at the European Southern Observatory, Paranal, Chile, 077.D-0011(A) and on observations obtained with *XMM-Newton*, an ESA science mission with instruments and contributions directly funded by ESA Member States and NASA.

CN Leo (Gl 406) is a well-known nearby flare star with a spectral type of M5.5 (Reid et al. 1995) or M6.0 (Kirkpatrick et al. 1991). In May 2006 it was the target of multi-wavelength observations carried out with VLT/UVES for the optical and *XMM-Newton* for the X-ray regime. During this observing campaign CN Leo was caught in a spectacular flare. An overview of the observed optical spectra can be found in Fuhrmeister et al. (2008), including an emission line list. The X-ray data are presented in Liefke et al. (2010). Here we use the optical high-resolution UVES spectra for comparison to a grid of flaring chromosphere models computed with the stellar atmosphere code PHOENIX. Our paper is structured as follows: in Sect. 2 we give a short description of the observations and data analysis. In Sect. 3 we characterise the construction and calculation of our chromospheric models. Our results from the comparison between models and data can be found in Sect. 4. Our conclusions are found in Sect. 5.

2. Observations and data analysis

The observations used in this paper were obtained in the context of a simultaneous multi-wavelength campaign with *XMM-Newton* and ESO's Kueyen telescope equipped with the Ultraviolet-Visual Echelle Spectrograph (UVES) on three half nights in May 2006: May, 19/20 (first night), 21/22 (second night), and 23/24 (third night).

The UVES spectrograph was operated in dichroic mode, producing a blue arm and a red arm spectrum. For the blue arm, a standard setup with central wavelength at 3460 Å was used, while in the red arm the standard setup with central wavelength at 8600 Å was slightly modified (blue-shifted) to cover Hα. The specific setup led to a spectral coverage from 3050 Å to 3860 Å in the blue arm and 6400 Å to 10080 Å in the red arm with a small gap from 8190 Å to 8400 Å caused by the CCD mosaic in the red. We used a slit width of 1″ resulting in a resolution of ~40 000.

The UVES spectra were reduced using the IDL-based `REDUCE` reduction package (Piskunov & Valenti 2002). The wavelength calibration was carried out with Thorium-Argon spectra and resulted in an accuracy of ~0.03 Å in the blue arm and ~0.05 Å in the red arm. Absolute flux calibration was carried out using the UVES master response curve and extinction files provided by ESO.

The flare we attempt to model here occurred at the beginning of the night of May, 19/20. A detailed description of the observations can be found in Fuhrmeister et al. (2008). The flare consists of a first sharp peak lasting only a few seconds, but increasing the flux by a factor of about 550 in the UVES blue photometer arm, followed by a broader second peak, which we attempt to model. Unfortunately the H_α line is saturated for our observations during the flare and therefore cannot be used for the modelling, but the blue arm covers the Balmer jump and the Balmer lines from H_9 on. The exposure times for the red arm spectra are 200 s and 1000 s for the blue arm spectra. Following the designation in Fuhrmeister et al. (2008) the broad flare peak is covered by blue spectrum No. 3 and red spectrum No. 9. The exact exposure times are found in Table 1. Note that the blue flare spectrum No. 3 covers the red arm flare spectra Nos. 9, 10, and 11, which are used for the modelling. Therefore, especially the blue arm spectra can unfortunately not be considered as "snapshots" of the flaring atmosphere.

3. Model construction and calculation

We used the PHOENIX atmosphere code v15.4 (Hauschildt et al. 1999) to model the flaring atmosphere of CN Leo. PHOENIX has already proven well-suited to computing M dwarf chromospheric models by Fuhrmeister et al. (2005b), who give a detailed description of the construction of chromospheric models. Since our current flare models are similarly constructed, we give only an overview of the construction and point out the differences to the treatment of the "quiescent" chromospheres.

A huge advantage of the PHOENIX code for chromospheric modelling is its ability of handling large sets of NLTE species, which is particularly important for M dwarfs; nonetheless a drawback of our PHOENIX chromospheric models is that all lines can currently be computed under the assumption of complete redistribution. Partial redistribution is generally important for strong lines such as Lyα and the Ca II H and K line, which we, however, do not use in our comparison.

3.1. Basic model parameters

Our 1-dimensional models consist of an underlying photosphere in radiative equilibrium, a chromosphere, and part of the transition region (TR) with a given temperature rise. For the underlying photosphere, a model with $T_{\rm eff} = 2900$ K and $\log g = 5.5$ and solar chemical composition (Grevesse & Sauval 1998) was used. These photospheric parameters were determined in our previous studies using PHOENIX photospheric models (Fuhrmeister et al. 2007, 2005b).

We computed our chromospheric models in hydrostatic equilibrium on a given column mass grid including convection and turbulent pressure. For the description of the turbulent pressure we chose a turbulent velocity of 2 km s^{-1} in the photosphere and of 0.5 $v_{\rm sound}$ throughout the chromosphere and TR, resulting in a turbulent velocity of about 5 km s^{-1} in the mid-chromosphere.

For the chromospheric and TR part of the models, we use a linear temperature rise vs. log(column mass) with different gradients in the chromosphere and TR. The TR extends up to $\log T = 5.0$. The top of the chromosphere is chosen at 8000 or 8500 K in our models, where 8000 K corresponds to the value chosen in previous modelling (Fuhrmeister et al. 2005b) for quiescent chromospheres, since for higher temperatures hydrogen is no longer an efficient cooling agent (Ayres 1979). In this study we also took models into account with a slightly higher temperature at the top of the chromosphere, since the flare is expected to heat the higher layers of the chromosphere in particular.

Since the correct NLTE modelling of lines is especially important for chromospheric models, we incorporated a large NLTE line set and did not use LTE lines, in contrast to our previous computations of M dwarf chromospheric models (Fuhrmeister et al. 2005b) following instead our findings for solar chromospheric models (Fuhrmeister et al. 2006). LTE lines are always over-predicted when included in the chromospheric part of the model and may pump the Lyman continuum, which in turn influences the strength of the hydrogen lines. In our previous study we therefore artificially included scattering of the LTE background lines by choosing the parameter ϵ in the relation $S = \epsilon B + (1 - \epsilon)J$. ϵ at intermediate value of 0.1, which should be appropriate for the mid-chromosphere. In the higher chromosphere and TR, this value should be much lower: $\epsilon \sim 10^{-4}$ (Anderson 1989; Falchi & Mauas 1998). Since this value of ϵ is unrealistic in the photosphere and most parts of the chromosphere, we decided against including LTE lines – which makes large NLTE line sets even more important for the model

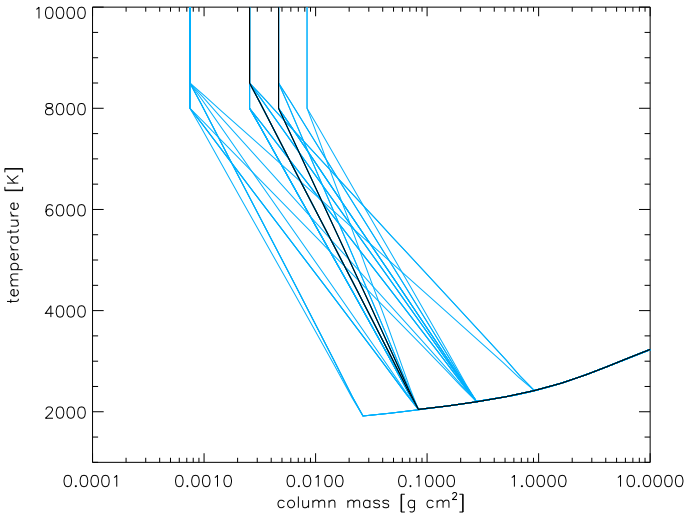

Fig. 1. Temperature vs. column mass distribution for our flare models. The two thick black lines denote the best-fit model for the blue and the red arm, respectively. The model with transition region onset at higher column mass is the best-fit model for the blue arm.

calculations, as well as for a good description of the spectra. Specifically, our modelling treats all lines from the ionisation stages of H I, He I-II, N I-VI, O I-VI, S I-VI, Ca I-III, Mg I-III, K I-II, Fe I-III, and Cr I-III in NLTE, where we use the levels from the newest Kurucz database[1] (older versions published e.g. by Kurucz & Bell 1995).

3.2. Flare spectra modelling

We computed a grid of 41 "flaring atmosphere" models. The temperature versus column mass distribution for these flare models is shown in Fig. 1. Fit parameters are (i) the log(column mass) at the temperature minimum ($\log cmass_{Tmin}$ varying from –0.1 to –1.5) and (ii) at the top of the chromosphere ($\log cmass_{Tchrom}$ varying from –2.1 to 3.1), (iii) the gradient in the TR ($\log \frac{dT}{d\log cmass}$ varying from 10.5 to 11.5), and (iv) the temperature at the top of the chromosphere ($T_{\rm chrom}$ varying from 8000 to 8500 K).

Following the approach of Mauas & Falchi (1996) and Fuhrmeister et al. (2005a), we built model spectra as a linear combination of the spectrum of the quiescent star and the flare model spectra, and compared these combined models to the observed flare spectra. This ansatz relies on the assumption that the flare covers only a small portion of the observed hemisphere, and therefore does not significantly alter the quiescent part of the emission. For our data of the CN Leo flare we already know that this assumption is true at least for the photospheric flare area. From the observations of blackbody radiation throughout the optical range (which should originate in the photosphere) during flare peak, we inferred a flare area of $1-10 \times 10^{18}$ cm^2, which is indeed very small compared to the stellar surface area (Schmitt et al. 2008). Assuming a radius of 0.1 $R_\odot$ for CN Leo, the coverage fraction of the flare is less than a percent.

For the linear combination we used the observed CN Leo spectrum directly before the flare as quiescent spectrum (taken at UT 23:13). At that time directly before the flare, the star was in an extraordinary low state of activity. We compared the amplitude of chromospheric emission lines to previous spectra taken in December 2005 and to the spectra an hour after the flare and found that the amplitudes were extremely low before the flare, very high in December 2005 and somewhat intermediate after the flare. Therefore, the non-active state of CN Leo is far from being constant, because of e.g. active regions present on the stellar surface. Since our spectra represent only some "average" flare atmosphere because of the long integration times, we decided to also use an post-flare spectrum as a quiescent mixing spectrum (see Sect. 4.1).

Since we want to linearly combine a synthetic spectrum with an observed one, we have to normalise one or both of them. We used two different methods of normalising the PHOENIX spectra: the absolute normalisation and the local normalisation. For the absolute normalisation the PHOENIX spectra are normalised overall using the known distance to CN Leo and radius estimates of 0.1 and 0.2 solar radii, since the true radius of CN Leo is not known (and, furthermore, there are rather large uncertainties in the absolute flux calibration of the observed spectra). In this case the whole observed spectral range was used for the comparison. For the local normalisation, the PHOENIX spectra are just normalised locally to the observed flux level of CN Leo (avoiding the problem of radius estimate and absolute flux calibration). Thus the level of the continuum emission is not used for the fit; only the emission lines are. Therefore, we did not use the complete spectral wavelength range with this normalisation method but selected wavelength ranges with strong emission lines. We used the following wavelength ranges for the comparison in the blue arm: 3150–3170, 3180–3200, 3200–3220, 3220–3230, 3250–3270, 3290–3315, 3325–3340, 3420–3435, 3535–3545, 3600–3625, 3635–3650, 3680–3700, 3700–3715, 3715–3755, 3775–3810, 3818–3833, especially covering, e.g., diverse Balmer and Alkali lines, one He II line, Fe I, and Fe II lines. In the red arm we used the following wavelength ranges: 6450–6500, 6660–6700, 6810–6860, 7060–7100, 7680–7720, 7760–7790, 8494–8543, 8650–8690, 9050–9100, 9210–9250, 9250–9300, 9530–9580, 10 000–10 082, covering, e.g., Alkali and Paschen lines, O I, He I, Fe I, and Fe II lines.

After obtaining a normalised linear combination model, we used a χ^2 algorithm to actually compare these models to our observed flare spectra. We investigated different linear combinations corresponding to different filling factors of the flare. We considered filling factors of 0.4, 0.3, 0.2, 0.15, 0.1, 0.07, 0.05, 0.03, 0.01, 0.005, and 0.001. For each filling factor the mean of the χ^2 for the different wavelength ranges were computed, and the lowest value then corresponds to the best filling factor for the individual model. These wavelength-averaged mean χ^2 values are compared for every model, thus finding the combination of best model and filling factor. For the different wavelength intervals, the best χ^2 can vary widely from about 1 to 3 to more than 50 for wavelength ranges containing major emission lines not computed by the code or emission lines that are poorly described by the models. The best mean χ^2 values for the different wavelength intervals vary accordingly between 5 and 20.

Using a χ^2 technique for finding the best-fit model rather than judging by eye has the advantage of being objective. We are aware that, especially for the absolute normation where the whole spectrum is used for the fit, this method overestimates the influence of the continuum. Therefore it provides a good fit for the photosphere, but may fit the chromosphere worse. For the local normalisation, this problem should be much less severe, since we use only narrow wavelength ranges with many and/or strong emission lines. This point is illustrated further in the discussion about the blue spectrum No. 3 in Sect. 4. Nevertheless, an automatic determination of the best fit is necessary for us, since we want to use not only the strongest lines, but also the wealth of

[1] From http://kurucz.harvard.edu/

metal lines. These cannot be fitted equally well by the models and would confuse and hinder a good fit by eye. Moreover we want to compare a large set of models and filling factors. This is hard to do by eye in an objective and reproducible way. A further complication arises from the fact that the red and blue arm observations never cover the same time intervals; therefore, the blue and red arm spectra must be modelled separately.

4. Results

With both normalisation methods we obtain best-fit models with similar model parameters. All these best-fit models provide a fairly good overall description of the flare spectra, and especially the local normalisation provides a good description of the chromospheric emission lines during the flare. Since both normalisation methods give similar results, we used this to obtain an error estimate on the chromospheric model parameters. We used four different methods, and from it took the four best-fitting models for computing mean chromospheric parameters for the flare. The four different methods are: 1. absolute normalisation with radius of 0.1 $R_\odot$, 2. absolute normalisation with radius of 0.2 $R_\odot$, 3. local normalisation with the identification of the best χ^2 done by using the mean of χ^2 of all wavelength intervals, 4. like 3., but using the median instead of the mean for the identification of the best χ^2.

The thus inferred mean best-fit parameters with 1σ error estimates in parenthesis can be found in Table 1. For the blue spectrum, the two normalisation methods result in quite different filling factors. While the overall normalisation gives a filling factor of 0.3 ± 0.2 percent, the local normalisation results in a filling factor of 3.3 ± 0.7 percent. This striking difference is unique for the blue spectrum and can be explained by the two normalisation methods favouring the tracing of different parts of the atmosphere using a χ^2 technique. If the photosphere is not affected severely by the flare, both methods trace the chromosphere. If spectral photospheric features turn up, the overall normalisation mainly traces the photospheric features, while the local normalisation with its focus on emission lines still mainly traces the chromosphere. Blue spectrum No. 3 is dominated by continuum emission (plus emission lines) that can be fitted by a blackbody spectrum, and is interpreted by Fuhrmeister et al. (2008) following Hawley & Fisher (1992) as the reaction of the photosphere to heating by non-thermal particles. When applied to our fitting results, this would mean that chromosphere and photosphere exhibit different filling factors. For the other spectra and especially in the red part of the spectra, the influence of the "blackbody" emission is much less severe and does not affect our fits.

In Fig. 1 we show the two models that fit best the red and the blue arm, respectively.

For the local normalisation method, an example comparison between the model spectrum and the observed spectrum in the very blue is shown in Fig. 2, where one can notice a slightly different slope of the continuum, even in this small wavelength range. This change is caused by the "blackbody" emission, which is not taken into account with the local normalisation method. Another comparison between model and blue spectral data is shown in Fig. 3, which includes two hydrogen Balmer lines. For the high members of the Balmer series one clearly notices quite a large discrepancy between model and observed spectrum in the line cores. One should keep in mind, though, that the best-fit model was found by fitting over wavelength ranges of large parts of the blue spectrum. Indeed one can find model spectra and filling factors that describe the Balmer lines much better, but give a poorer fit in other spectral ranges.

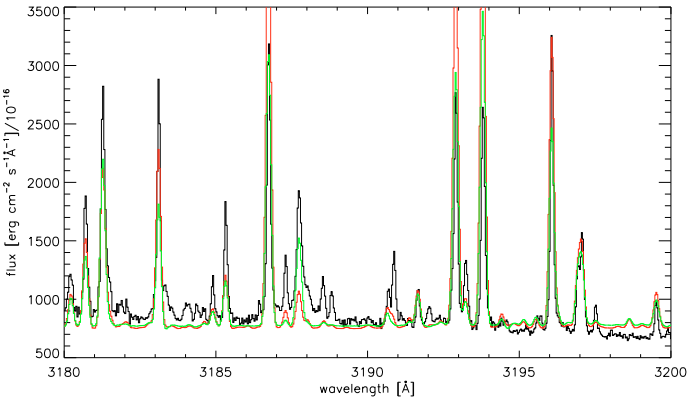

Fig. 2. Comparison of the blue best-fit linear model (green/light grey) to our data (black) for the local normalisation for a wavelength range in the very blue part of the spectrum. The dominant lines are due to Ca II, Fe II, and Cr II. Additionally in grey/red the best-fit model of our non-linear models is shown.

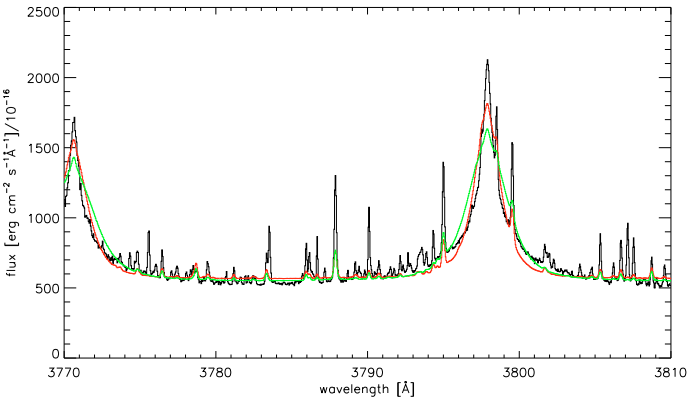

Fig. 3. Comparison of the blue best-fit linear model (green/light grey) to our data (black) for the local normalisation. In grey/red the best-fit model of our non-linear models is also shown. The two broad lines are H_{10} and H_{11} from the Balmer series.

Also, the metal lines which directly neighbouring the Balmer lines are too weak compared to the Balmer lines (so the metal lines alone would predict even higher filling factors). This already illustrates the difficulty of fitting large elemental sets and large spectral ranges well with just one model.

For the red arm two comparison between data and model are shown in Figs. 4 and 5 for an He I line and a K I line also for the local normalisation. Here again, other models than the above-defined "best-fit" model can give better representations of individual lines; for example, the emission core of the K I line is described much better with a slightly higher filling factor as can be seen in Fig. 5. In general, the line core becomes stronger for models with the temperature minimum at higher column mass, i.e., at deeper layers of the atmosphere. Therefore, models with the temperature minimum at even higher column mass than for the strongest models in our grid may also give a better representation of the line. Also, a steeper temperature rise leads to a stronger K I emission core. Since the line arises from the mid to lower chromosphere (see Sect. 4.3), a steeper rise in these layers of the atmosphere should increase the K I emission core, without altering the emission from lines arising in the upper chromosphere/transition region like the Balmer lines too much. Therefore, models with a more sophisticated temperature rise, i.e., a non-linear temperature rise in the chromosphere, should lead to a better simultaneous description of more lines.

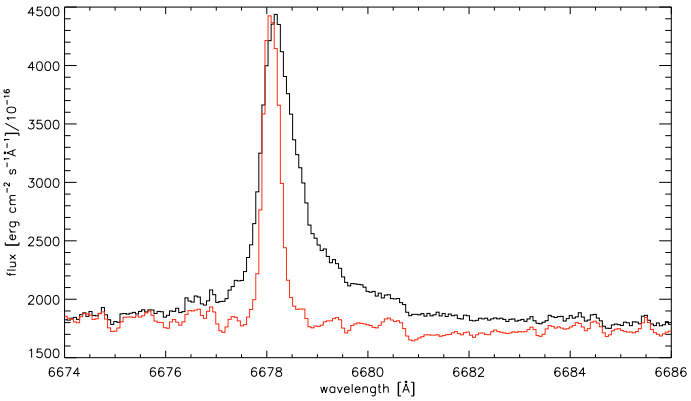

Fig. 4. Comparison of the red best-fit model (red/grey) to our data (black) for the local normalisation for a strong He I line at 6678 Å showing an asymmetric line broadening from about 6674 to 6684 Å.

Unfortunately, e.g. strong Fe lines do react to both: altering the temperature structure in the lower, as well in the upper, chromosphere. This complicates building a unique best-fit model. We therefore restricted our study to the simpler case of finding the best-fit in a parametrised model grid. Also constructing a semi-empirical temperature rise in conjunction with the use of a filling factor may lead to non-uniqueness of the best fit due to too many free parameters. Moreover one should keep in mind that our observed spectra are integrated in time over significant fractions of the flare duration, so that the real spectra can be assumed to change during the exposure time. Since different chromospheric emission lines react on different timescales during flares, this may also lead to the situation, where different models are needed for the description of different lines.

For the He I line, the line width is not fitted correctly. Concerning the line broadening of the here presented flare data, the He I lines exhibit extreme broadening (from about 6674 to 6684 Å) and asymmetries, which lead to more observed flux in the red wing. This phenomenon is seen in Fig. 4 as the additional flux red of the observed line. It is even more easily seen if the quiescent flux is subtracted from the flare spectra. The additional flux can be described well by an extremely broad and red shifted Gaussian line. The line asymmetries are discussed in Sect. 4.3 and in detail by Fuhrmeister et al. (2008). Since the additional red-shifted line flux is interpreted as caused by mass motions, the line width cannot be described correctly by our simple (static) models.

As an example of the overall normalisation we show part of the blue arm spectrum and the best overall fit model for 0.2 $R_\odot$ in Fig. 6. Too much emission around the end of the Balmer series is seen in this example. This is also true for all other flare models with the chromosphere located deep in the atmosphere and (resulting) low filling factors. For models with their chromospheres further out and higher filling factors, the problem is less severe. Nevertheless, the overall fitting process favours models with the chromosphere deep in the atmosphere, since for models with weak Balmer jumps, the corresponding emission lines are too strong (since for these models the emission lines relative to the continuum have smaller amplitudes).

Although our best-fit models provide a fairly good overall fit, individual lines may require slightly different models or filling factors mostly within the error we estimated for our best-fit model. Nevertheless, together with the poor characterisation of features like the Balmer jump, this points to basic problems with our simple models. A better description of the data can most probably be achieved with a non-linear temperature rise in the chromosphere and a height-dependent filling factor, which are both beyond the scope of this paper. Another problem is that we use static models for a dynamic atmosphere. A more physical description should include e.g. dynamic ionisation, especially for flares. For the solar chromosphere, the effect of dynamic hydrogen ionisation due to propagating shocks was shown by Carlsson & Stein (2002), who found that the relaxation timescales are in the order of 10^3 to 10^5 s in the chromosphere and therefore longer than dynamical timescales. Also, ionisation in shocks is more rapid than recombination behind them, causing the electron density to represent the higher temperatures of shocks. Similar arguments should be valid for flare events like the one on CN Leo.

Therefore, the detected mass motions during the flare and phenomena like the blackbody emission caused by non-thermal particles led us to conclude that eventually a far more sophisticated treatment including hydrodynamics in 1D or 3D is required for a more physical flare modelling.

4.1. Temporal evolution

Besides fitting of the spectrum covering the broad flare peak we also fitted the consecutive spectra in the decay phase. Moreover we tried to fit the spectra covering the flare onset. For the latter the assumption of hydrostatic equilibrium should break down, especially for the red arm spectrum No. 8, which covers about the first 10 s of the flare, while the blue spectrum No. 2 covers the first minute of the flare. We nevertheless tried to find fitting models for the flare onset, however, for the red spectrum No. 8 no meaningful fit could be established as expected. Especially the continuum and line fitting method lead to contradicting results: the line fit method leads to best-fit models with chromospheres located further out, since the lines react not as fast as the continuum to the flare onset and many lines have not yet gone into emission in spectrum No. 8.

For the blue spectrum No. 2 similar mean fit parameters as for spectrum No. 3 are found in the fit, but for the local normalisation method for different wavelength ranges different filling factors are preferred by the fit. Therefore, the different emission lines dominating the individual wavelength ranges used for the fit lead to different filling factors, indicating that the fit does not give a stable result. Therefore, no meaningful fit for the blue spectrum No. 2 could be obtained.

For the decay phase, two additional red spectra (Nos. 10 and 11) are used. Although in the red spectrum No. 12 some emission lines are still elevated, the majority of the lines have vanished and also the continuum emission has returned to its quiescent value. The blue arm clearly reacts longer to the flare (see also Fuhrmeister et al. 2008). This is especially true for the chromospheric emission lines. While the continuum has already returned almost to its quiescent value, most of the emission lines stay still elevated for blue spectrum No. 4. Therefore the usage of blue spectrum No. 4 is possible, when applying only the line fitting method. Since the overall fitting method is dominated by the influence of the continuum, no flare is found any more: the filling factor obtained for the flare in this case is 0.005 percent and the fit leads to very similar values of χ^2 for most of the models. In the blue spectrum No. 5 the quiescent level is reached also for the emission lines. We give the best-fit parameters for the decay phase spectra obtained as discussed in Sect. 4 in Table 1; with the 1σ standard deviations in parentheses.

Using instead a post-flare spectrum as the quiescent mixing spectrum, we find slightly different best-fit parameters, which

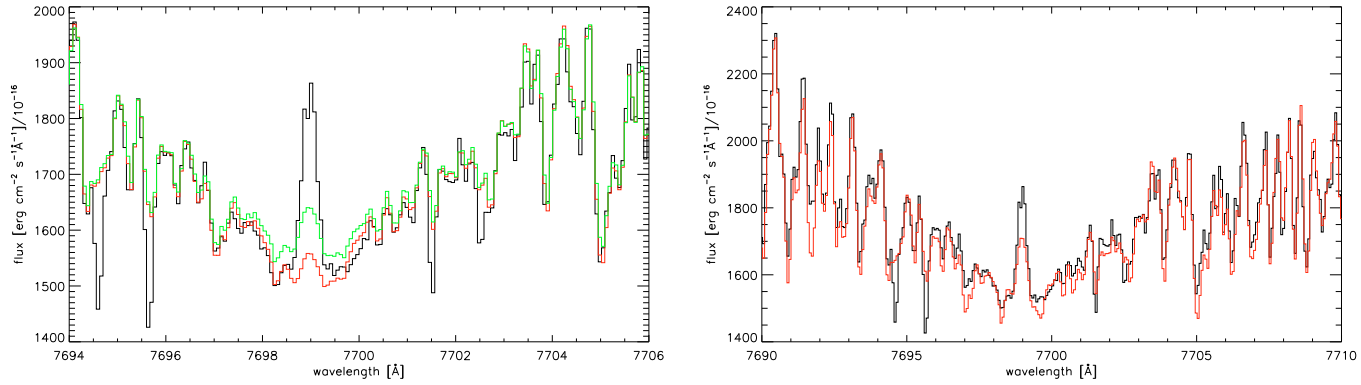

Fig. 5. *Left*: comparison of the red best-fit model (red/grey) to our data (black) for the local normalisation for a K I line While the (photospheric) absorption wings of the line are described well, the emission core is by far too weak in the model. Additionally in light grey/green the best-fit model of our non-linear models is shown. *Right*: the same model, but with a filling factor of 10 instead of 3 percent.

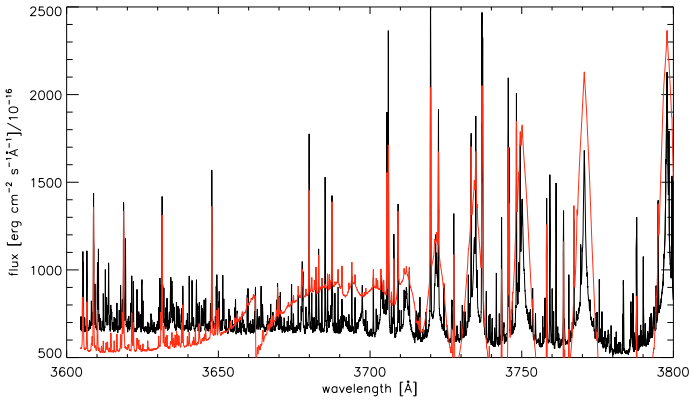

Fig. 6. Comparison of a strong blue model (red/grey) to our data (black) for the overall normalisation.

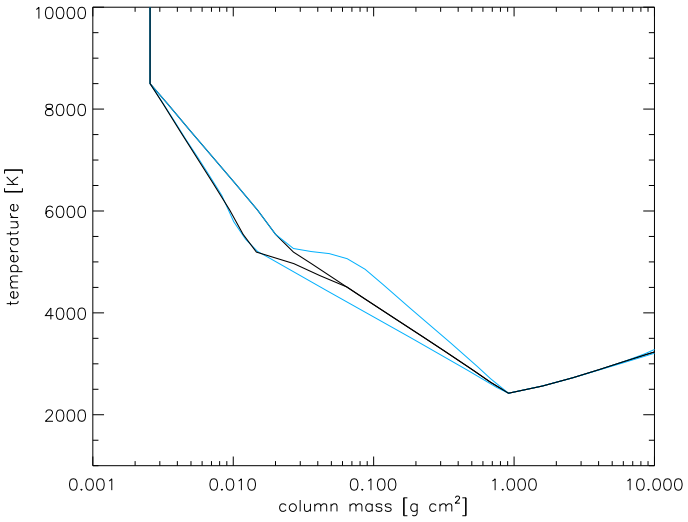

Fig. 7. Temperature vs. column mass distribution for the non-linear models. The black/heavy lines denote the best-fit models; the model which extends further out in the atmosphere is the blue arm best-fit model.

nevertheless agree within the errors. Since the post-flare spectrum is a bit more active we find a tendency towards lower filling factors, as expected. Our fit results seem to be quite robust against such small perturbations, although the fit quality may be quite different for individual lines.

Moreover, the mean chromospheric flare parameters are quite stable throughout the flare. Nevertheless, there seems to be a trend in the filling factor: for evolved flare spectra the flare filling factor becomes smaller. On first glance this somewhat contradicts the picture of the flare plasma spreading out over time; however, since spreading also means cooling, the filling factor of the hot component should indeed become smaller. According to our simulations, this hot component, nevertheless, still dominates, or at least describes the observed spectra best.

4.2. Non-linear models

Besides our studies of the flare using models with a linear temperature rise, we computed four models where we released this constraint and used linear segments instead. The temperature distributions for these models can be found in Fig. 7. We constructed the non-linear models to see which improvements can be achieved simply by building some sort of linear combinations of two good fitting models (linked either directly or by some sort of plateau). We tried to improve the fitting of as many lines as possible for one spectrum by releasing the linear constraint. We do not intend to construct a model like the VAL model for the Sun (Vernazza et al. 1981), though. This is beyond our scope and beyond the data. (Since the red and blue arm represent not the same flare state, both are heavily integrated and the flare filling factor complicates the situation)

Naturally, releasing the linear temperature gradient constraint should lead to better fitting models, since the number of possible solutions is enlarged. Nevertheless, we find that for the four non-linear models we constructed, the best-fit non-linear model does not give as good a fit as the best-fit model with linear temperature distribution. This applies to both the blue and the red arm spectra. Nevertheless, our non-linear models lead to the same filling factor as our linear models. Moreover, they give an improved description of the Balmer lines. The worse overall fit comes from the wealth of metal emission lines included in the line-fitting process, out of which many are formed at intermediate temperatures (see the two Fe I lines in Table 2 as an example). These lines are directly influenced by the changed temperature distribution, but should also react to NLTE effects. Fit examples can be found in Figs. 2, 3, and 5 for the extreme blue part of the spectrum, two Balmer lines and one K I line. For the Balmer lines, the fit is improved compared to any linear model. Nevertheless, for the extreme blue part of the spectrum with the wealth of metal lines, the non-linear model does not give

Table 1. Overview of the mean flare fit parameters in time.

Spectrum	Observation time	$T_{\rm chrom}$	$\log cmass_{T\rm chrom}$	$\log cmass_{T\rm min}$	grad TR	Filling factor
blue No. 3	UT 23:48:16–00:04:56	8100 (200)	–2.3 (0.1)	–0.7 (0.3)	11.1 (0.3)	3.3 (0.7)/0.3 (0.2)
red No. 9	UT 23:47:37–23:50:57	8300 (200)	–2.6 (0.3)	–0.7 (0.3)	11.0 (0.2)	2.2 (1.1)
red No. 10	UT 23:51:56–23:55:16	8300 (200)	–2.7 (0.2)	–0.6 (0.3)	11.1 (0.3)	0.7 (0.3)
red No. 11	UT 23:56:14–23:59:24	8200 (300)	–2.7 (0.3)	–0.7 (0.4)	11.1 (0.3)	0.06 (0.02)
blue No. 4	UT 00:05:46–00:22:26	8300 (300)	–2.7 (0.3)	–0.9 (0.2)	11.2 (0.3)	0.1 (0.0)

a better fit. In the red spectrum for the K I line for the non-linear model, a higher central emission peak can be noticed, which makes the fit better. On the other hand, for the innermost wings of the line, the non-linear model gives too much flux, which makes the fit worse. This again is caused by the changed temperature distribution of the non-linear model in the formation region of the line and can be also noted in some of the models with similar linear temperature distribution in the lower chromosphere. Therefore, our four non-linear models still fail to give a better description of the wealth of emission lines. This does not mean, however, that there are no non-linear models that can achieve a better fit for more lines. With only small pertubations of the linear temperature distribution it is nevertheless possible to achieve better fits of groups of lines, such as the Balmer lines. But trying to fit more and more lines simultaneously makes the situation very complicated, because of both the NLTE effects and the binning of the filling factor.

4.3. Depth of line formation

During the flare peak and the decay phase, additional line flux occurred in the red wings of several lines. These line asymmetries were found for Balmer lines, He I, and Ca II lines, as discussed by Fuhrmeister et al. (2008). The asymmetries were ascribed to a moving "cloud" in the stellar atmosphere, not unlike a chromospheric downward condensation, as known from the Sun. Those lines showing these asymmetries – in contrast to the majority of lines, which do not show asymmetries – are all predominantly formed in the upper chromosphere and onset of the transition region. A more detailed analysis is possible with the context of PHOENIX models of the flaring atmosphere of CN Leo, so that constraints for the conditions can be obtained under which individual lines are formed; therefore, we can determine the main parameters of the moving cloud (such as temperature and density).

The crucial parameter for such a study is the atmospheric depth, from which most of the flux of an individual line arises. This line formation depth can be assessed via the contribution function $\mathscr{C}_F$, which is implemented in PHOENIX (Fuhrmeister et al. 2006). Since we take into account only strong lines, the flux contribution function is a useful approximation to the line depression/raise contribution function (Magain 1986). As an example of line formation as traced by the flux contribution function we show $\mathscr{C}_F$ for line centre, wing and continuum for the Ca II line at 8500 Å and for the K I line at 7699 Å in Figs. 8 and 9. As expected, the line formation depth moves outward for wavelengths approaching line centre. The nearly vertical drop of the contribution function at low column mass (found in both figures) is due to the transition region, where the density drops rapidly (see also Fig. 10).

Since the line opacity is highest at the line-centre, we determined the line centre line formation depths for various lines, including the lines showing asymmetries during the flare. The estimated formation temperatures for various lines are listed in Table 2, and we quote the corresponding temperature for the maximum of the contribution function in parentheses; the two He I lines have such broad and flat peaks in the contribution function that no useful maximum can be defined, hence no corresponding temperature range.

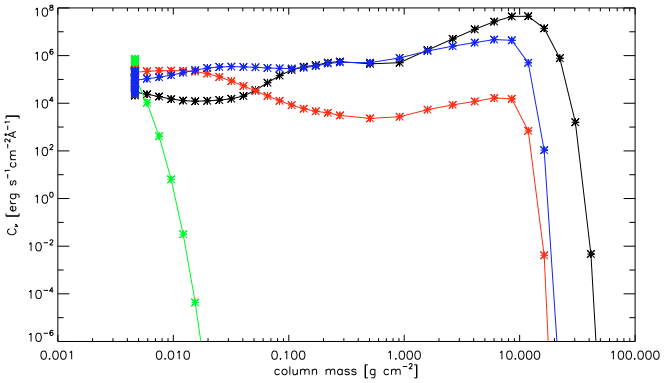

Fig. 8. Contribution function for the Ca II line at 8500 Å. The black curve denotes the continuum, the blue curve the line wing, the red curve the line maximum, and the green curve the line reversal/centre. The asterisks mark the actual layers in our model.

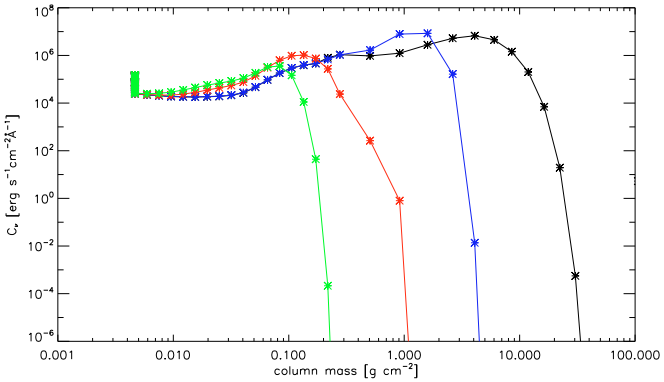

Fig. 9. Contribution function for the K I line at 7699 Å. The black curve denotes the continuum, the blue and red curves denote the line wing, and the green curve denotes the line centre.

As far as the line asymmetries are concerned, we note that all these lines have quite broad peaks in their contribution functions, but with maxima corresponding to temperatures between 8000 and 9500 K. Although other lines with broad formation peaks like Fe II may form at similar temperatures, their formation maximum is either at lower or higher temperatures. Under the assumption that the moving cloud responsible for the asymmetries has similar densities to the formation regions in our chromospheric model, we can estimate the temperature of the moving gas cloud to be about 8000 to 9500 K (as was indeed our initial guess, see Fuhrmeister et al. 2008).

Table 2. Formation temperatures of various emission lines.

Ion	Wavelength [Å]	Formation temperature [K]
Fe I	7068.42	3300–4500 (3900)
Fe I	7748.28	3600–4500 (4200)
K I	7698.98	4200–5100 (4600)
Ca II	8498.02	8500–10 900 (8500)
He I	6678.15	8500–25 200
He I	7065.19	8500–25 000
H I	6562.82	8500–12 000 (8500)
H I	10049.38	8500–15 700 (8500)
H I	3711.97	8000–15 300 (9100)
H I	3703.86	8000-15 300 (9200)
O I	7771.96, 7774.18,7775.40	9000–13 200 (10 900)
Fe II	3226.81	8000–14 200 (11 700)

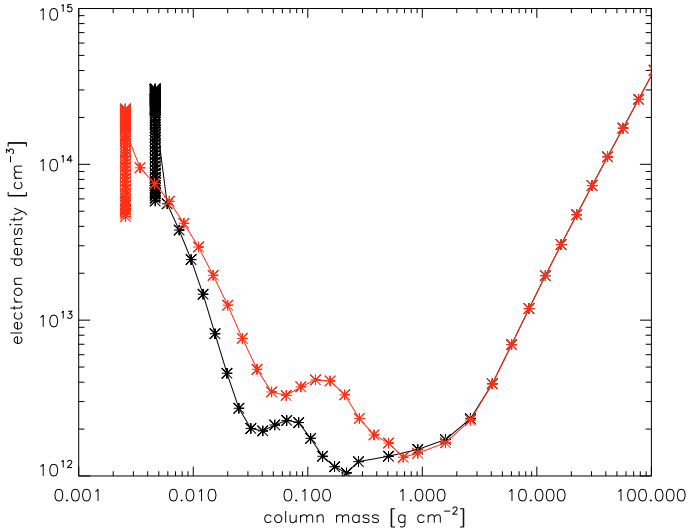

Fig. 10. Electron density for the two best-fit models. The black curve denotes the blue arm best model, while the red/grey curve denotes the red arm best model.

If one assumes that the origin of the moving material is about the onset of the transition region as suggested by the derived temperatures, a formation height of the moving gas can be determined from the models. Because of the high log g in our models the onset of the transition region is only about 100 km above the photosphere. Other chromospheric flare models for AD Leo with a lower log g derive heights of about 500 km above the photosphere (Mauas & Falchi 1996). For the moving material velocities of about 20 km s^{-1} (with a large scatter) have been derived (Fuhrmeister et al. 2008). The asymmetries can be recognised in at least 3 spectra corresponding to an observing time of at least 600 s, or even more for the case of the Hα line. If the moving material would consist of a single cloud it could move more than 10 000 km. If the above suggested origin of the moving material is correct, only a multitude of downflows can account for the asymmetries (which was already suggested by the variations in the asymmetry of the Hα line, Fuhrmeister et al. 2008).

4.4. Electron density

We find in our models of the flaring chromosphere rather high electron densities throughout the chromosphere (see Fig. 10) for our two best-fit models from the local normalisation method, but similar results hold for the overall normalisation method. The electron number density in the upper chromosphere and lower transition region is in excess of 10^{14} cm^{-3}. The maximum of the electron number density as seen in Fig. 10 occurs in the lower transition region at around 13 000 K. The steep temperature rise in the TR means that the distribution of the electron density in Fig. 10 is nearly vertical. Close inspection reveals that the electron density is still rising in the lower TR followed by a sharp drop.

Models of very active, but quiescent chromospheres of M dwarfs show that the electron density peaks about 10^{11}–10^{12} cm^{-3} (Mauas & Falchi 1994; Short & Doyle 1997). Hawley & Fisher (1992) found electron densities of about 10^{13} cm^{-3} in the upper chromosphere in her flaring models. For a large flare on AD Leo Mauas & Falchi (1996) determined electron densities of about 10^{13} cm^{-3} for their best-fitting model, but got also densities of about 10^{14} cm^{-3} for another model.

In the Balmer series Hα (in the red arm) and H$_9$ to H$_{18}$ (in the blue arm) are observed. Even higher Balmer line members up to H$_{24}$ have been reported for CN Leo (Fuhrmeister et al. 2004). These recover during the course of the night after the flare up to H$_{23}$. During the flare onset spectrum No. 2, even fewer Balmer line members can be detected (up to H$_{14}$). This comes from the merging of the lines due to Stark broadening, which is stronger for higher densities during flares (Švestka 1972). The same is true for the Paschen series. In the flare onset red spectrum No. 8 the Pa 7 line may be present, while in the spectrum No. 9 clearly Paschen lines up to Pa 12 are present. Using the Inglis-Teller formula from Kurochka & Maslennikova (1970) relating the highest resolved line into an electron pressure, this leads to log(n_e) = 14.0 for the blue spectrum No. 2 and to log(n_e) = 13.2 for the blue spectrum No. 3, while for the red spectrum No. 9 log(n_e) = 14.4 is obtained.

Because the flare exhibited such high chromospheric densities, we would also expect high coronal densities. During the quiescent state, coronal electron densities of about 10^{10} cm^{-3} have been determined for CN Leo using X-ray observations by *XMM-Newton* (Fuhrmeister et al. 2007). In this study of smaller flares, a tentative density increase has been measured, though the obtained density values are in agreement with the quiescent ones when accounting for the errors. For the present giant flare multi-wavelength data with *XMM-Newton* have also been obtained, and we determined coronal densities of at least 10^{12} cm^{-3} (Liefke et al. 2010). Therefore, the giant flare leads to very high electron densities in both the corona and the chromosphere.

5. Summary and conclusion

We constructed a set of 41 "flaring chromospheric" models and find that the synthetic spectra characterise the observed flare spectra quite well for the flare peak when using filling factors of about 2–3 percent for the chromosphere. From the blue spectrum we also find a filling factor of about 0.3 percent for the photospheric part of the flare in rough agreement with values derived from photometry. The flare models indicate that both the chromosphere and the photosphere are strongly heated during the flare. The chromosphere is shifted to much higher column masses and the temperature rise is much steeper compared to a chromospheric model of the quiescent atmosphere of CN Leo (Fuhrmeister et al. 2005b). During the decay phase, the best-fit parameters suggest that the filling factor of the flare area is declining.

The inferred different filling factors for chromosphere and photosphere support the idea of height-dependent filling factors.

Similar results were found by Hawley & Fisher (1992) for a large flare on AD Leo. From the chromospheric lines, they derived a filling factor of about 10 percent, while they found a filling factor of about 0.02 to 0.5 percent from the continuum black body fit. Also for the Sun, the flare area of white light-flares is smaller than the one covered by Hα kernels (Mauas 1990).

Comparison of our inferred chromospheric filling factor of about 2–3 percent during flare peak to the Sun (where the Hα flare area is normally 0.01 percent of the disk) shows it to be rather large. However, for stellar flares it is quite small. For example, Fuhrmeister et al. (2005a) found a filling factor of about 20 percent for a large flare on LHS 2034 (dM6) using the same technique as here. Mauas & Falchi (1996) found a filling factor of about 5 percent for a flare on AD Leo also utilising comparison to chromospheric models. Using a blackbody fit, Mochnacki & Zirin (1980) found a filling factor of about 2 percent for a flare on YZ CMi. Therefore, in the stellar context our inferred filling factor is quite small, which is especially remarkable, since the flare it is describing is a giant one.

Acknowledgements. B.F. acknowledges financial support by the DLR under 50OR0105.

References

Allred, J. C., Hawley, S. L., Abbett, W. P., & Carlsson, M. 2005, ApJ, 630, 573
Allred, J. C., Hawley, S. L., Abbett, W. P., & Carlsson, M. 2006, ApJ, 644, 484
Anderson, L. S. 1989, ApJ, 339, 558
Ayres, T. R. 1979, ApJ, 228, 509
Carlsson, M., & Stein, R. F. 2002, ApJ, 572, 626
Cram, L. E., & Woods, D. T. 1982, ApJ, 257, 269
Falchi, A., & Mauas, P. J. D. 1998, A&A, 336, 281
Fuhrmeister, B., Schmitt, J. H. M. M., & Wichmann, R. 2004, A&A, 417, 701
Fuhrmeister, B., Schmitt, J. H. M. M., & Hauschildt, P. H. 2005a, A&A, 436, 677
Fuhrmeister, B., Schmitt, J. H. M. M., & Hauschildt, P. H. 2005b, A&A, 439, 1137
Fuhrmeister, B., Short, C. I., & Hauschildt, P. H. 2006, A&A, 452, 1083
Fuhrmeister, B., Liefke, C., & Schmitt, J. H. M. M. 2007, A&A, 468, 221
Fuhrmeister, B., Liefke, C., Schmitt, J. H. M. M., & Reiners, A. 2008, A&A, 487, 293
Grevesse, N., & Sauval, A. J. 1998, Space Sci. Rev., 85, 161
Hauschildt, P. H., Allard, F., & Baron, E. 1999, ApJ, 512, 377
Hawley, S. L., & Fisher, G. H. 1992, ApJS, 78, 565
Houdebine, E. R. 1992, Ir. Astron. J., 20, 213
Kirkpatrick, J. D., Henry, T. J., & McCarthy, D. W. 1991, ApJS, 77, 417
Kurochka, L. N., & Maslennikova, L. B. 1970, Sol. Phys., 11, 33
Kurucz, R. L., & Bell, B. 1995, Atomic line list, Kurucz CD-ROM (Cambridge, MA: Smithsonian Astrophysical Observatory)
Liefke, C., Fuhrmeister, B., & Schmitt, J. H. M. M. 2010, A&A, submitted
Magain, P. 1986, A&A, 163, 135
Mauas, P. J. D. 1990, ApJS, 74, 609
Mauas, P. J. D., & Falchi, A. 1994, A&A, 281, 129
Mauas, P. J. D., & Falchi, A. 1996, A&A, 310, 245
Mochnacki, S. W., & Zirin, H. 1980, ApJ, 239, L27
Piskunov, N. E., & Valenti, J. A. 2002, A&A, 385, 1095
Reid, I. N., Hawley, S. L., & Gizis, J. E. 1995, AJ, 110, 1838
Schmitt, J. H. M. M., Reale, F., Liefke, C., et al. 2008, A&A, 481, 799
Short, C. I., & Doyle, J. G. 1997, A&A, 326, 287
Švestka, Z. 1972, ARA&A, 10, 1
Vernazza, J. E., Avrett, E. H., & Loeser, R. 1981, ApJS, 45, 635